Journal of Materials Research and Technology 36 (2025) 7881–7896

Contents lists available at ScienceDirect

Journal of Materials Research and Technology

journal homepage: www.elsevier.com/locate/jmrt

Texture multi-polarization and its impact on mechanical anisotropy in Mg-10Gd alloy

Dongsheng Han [a], Cai Chen [b,*], Benoit Beausir [c], Zhonghua Du [a], Sen Yang [d], Mingchuan Wang [b], Rui Ren [b], Fengjian Shi [e], Yuli Zhou [f], Wei Chen [f], Werner Skrotzki [g], Zhangzhi Shi [h], Laszlo S. Toth [c,i]

[a] School of Mechanical Engineering, Nanjing University of Science and Technology, Xiaolingwei 200, Nanjing, 210094, PR China
[b] Sino-French Engineer School, Nanjing University of Science and Technology, Xiaolingwei 200, Nanjing, 210094, PR China
[c] Laboratoire d'Etude des Microstructures et de Mécanique des Matériaux (LEM3), Université de Lorraine, CNRS, Arts et Métiers ParisTech, F-57045, Metz, France
[d] School of Materials Science and Engineering, Nanjing University of Science and Technology, Xiaolingwei 200, Nanjing, 210094, PR China
[e] School of Materials Science and Engineering, Jiangsu University of Science and Technology, Zhenjiang, 212003, PR China
[f] Chinalco Materials Application Research Institute Co.,Ltd. Suzhou Branch, Suzhou, 215026, PR China
[g] Institute of Solid State and Materials Physics, Dresden University of Technology, Dresden, 01062, Germany
[h] State Key Laboratory for Advanced Metals and Materials, School of Materials Science and Engineering, University of Science and Technology Beijing, Beijing, 100083, PR China
[i] Metal-forming and Nanotechnology, Institute of Physical Metallurgy, University of Miskolc, 3515, Miskolc, Hungary

ARTICLE INFO

Handling editor: L Murr

Keywords:
Mg–Gd alloy
Extrusion-shearing process
Mechanical anisotropy
Texture multi-polarization
Extension twin

ABSTRACT

The anisotropic mechanical properties of wrought Mg alloys are significantly influenced by their crystallographic texture. This study examines the impact of texture multi-polarization on the mechanical anisotropy of Mg-10Gd (wt.%) alloy, using conventional extrusion (EX) and extrusion-shearing (ES) processes. A multipolar texture distribution was successfully achieved through the ES process, including basal textures (<10-10> or <2-1-10> || extrusion direction (ED)), shear-induced B fiber texture (basal plane || shear plane), C-texture (<0001> || ED) and "Rare Earth" texture (*c*-axis || shear direction). The evolution of microstructure and mechanical properties of the processed samples under tension and compression were thoroughly investigated. At equivalent strain levels applied via both EX and ES processes, the ES samples demonstrated superior mechanical properties and isotropy. The yield stress and elongation to failure of ES sample under tension were 166.48 MPa and 23.33 %, that is 19.92 % and 50.41 % higher than those of EX sample. The compressive yield strength ratio between ED and normal direction of the ES samples reached 0.93, higher than that of the EX samples (0.77). This improvement is attributed to the more homogenized microstructure and the multipolar textures. Moreover, the effect of individual texture components on plastic deformation and yield strength were calculated by Visco-Plastic Self Consistent (VPSC) modeling. The results suggested that variations in the activation of {10–12} extension twins are the primary factor responsible for the mechanical anisotropy observed under compression. For the ES sample, the grains with *c*-axis tilted towards the shear direction or the shear plane normal benefit the reduction of anisotropy.

1. Introduction

Wrought magnesium (Mg) alloys exhibit excellent specific strength, stiffness, and low density, making them ideal structural materials for lightweight applications in aerospace, automotive, electronics, and various other fields [1–3]. However, Mg alloys have a hexagonal close-packed (HCP) crystallographic structure with low symmetry, which restricts the activation of slip systems during deformation at room temperature [4–6]. This restriction results inleads to poor ductility in wrought Mg alloys. Additionally, when processed by traditional deformation techniques, such as hot-rolling [7,8] and extrusion [9,10], strong basal textures are commonly formed in Mg alloys, leading to pronounced mechanical anisotropy [11]. As structural materials, wrought Mg alloys face challenges in industrial applications due to these

* Corresponding author.
E-mail address: cai.chen@njust.edu.cn (C. Chen).

https://doi.org/10.1016/j.jmrt.2025.05.030
Received 24 March 2025; Received in revised form 4 May 2025; Accepted 5 May 2025
Available online 9 May 2025

limitations. Improving the overall mechanical properties of wrought Mg alloys has become a primary focus in research on Mg alloys [11–14].

Grain refinement is one of the most important strategies used to enhance the strength and ductility of Mg alloys [15,16]. By applying a reasonable increase in strain through deformation processes, such as severe plastic deformation techniques [16,17], the average grain size of Mg alloys can be refined to below 1 μm [18,19]. According to the Hall-Petch relationship, significant grain refinement should substantially improve the yield strength of Mg alloys [20]. However, researchers have found that the strength improvement from grain refinement is not always as expected [21,22]. For example, while further grain refinement can occur following equal channel angular pressing (ECAP) of extruded Mg alloys [18], the yield strength may decrease unexpectedly. This phenomenon is primarily attributed to the transformation of the basal fiber texture in extruded Mg alloys into shear texture components after deformation by ECAP, leading to a texture softening effect [18,23,24]. Avoiding the formation of crystallographic textures in thermally deformed Mg alloys is particularly challenging [24]. In wrought Mg alloys, the texture dependence of deformation mechanisms along various loading directions is one of the main causes of mechanical anisotropy properties [14,25]. Therefore, controlling the texture while refining the grains is critical for developing Mg alloys with superior comprehensive mechanical properties [4,7,26].

Texture modification in wrought Mg alloys can be effectively achieved through the addition of rare earth (RE) elements [27]. Numerous studies [28–30] have demonstrated that alloying by RE elements not only provides significant solution strengthening and precipitation strengthening effects on Mg alloys, but also weakens the basal texture by promoting the formation of "RE-textures". For instance, RE-texture components of <2-1-12>−<2-1-14> || extrusion direction (ED) could replace the traditional <10-10> || ED basal component in extruded Mg–Gd alloys [31]. This alteration is beneficial for improving ductility and reducing anisotropy [32,33]. Applying shear deformation is also an effective method to alter control the deformation textures in Mg alloys. Beausir et al. [34] reported that following shear deformation via ECAP, multiple types of ideal shear texture components could develop in the alloy, including: basal plane || shear plane (B fiber), <a> || shear direction (P fiber), *c*-axis rotated towards the shear plane by 30° (Y fiber) and c-axis firstly rotated 90° in the shear direction then ±30° in the shear plane direction (C_1 and C_2 fiber), respectively. In recent years, the development of fine-grained microstructures with multipolar orientations has emerged as a vital method for achieving high-performance Mg alloy [35–37]. In this study, the presence of multiple crystallographic texture components with several orientation poles in {0002} pole figure of Mg alloy is defined as multipolar texture, and the process to introduce the multipolar texture distribution is referred to as texture multi-polarization. Compared to completely randomizing the textures, obtaining multipolar textures in Mg alloys is more feasible. For example, by employing combined deformation techniques such as rolling and compression [35], pre-tension and subsequent re-compression deformation followed by annealing treatments [36], applying rotary-die equal channel angular pressing (RD-ECAP) process [10,38,39], or the extrusion-shearing process [40], it is possible to achieve texture multi-polarization in Mg alloys. It was also reported [38] that the mechanical anisotropy of Mg alloys can be improved due to the presence of multipolar texture distribution. Nevertheless, research on multipolar texture in wrought Mg alloys remains scarce, and the influences of individual texture components on the deformation mechanisms during processing require further investigation.

In this study, we successfully prepared a Mg-10Gd (wt.%) alloy with distinct multipolar texture distribution by employing a composite deformation process consisting of extrusion followed by two ECAP passes in route C. This deformation process is referred to as extrusion-shearing (ES) process [41]. Compared to the sample obtained through conventional extrusion processing (EX), the ES-processed samples exhibit superior mechanical properties under tension and compression. Under compression, the ES process enabled the Mg-10Gd alloy to achieve excellent isotropic yield stress. To reveal the impact of multipolar texture distribution on mechanical anisotropy, polycrystal plasticity simulations were used to quantitatively evaluate the contributions of individual texture components to yield strength and their roles in deformation mechanisms under compression.

2. Experiments

The initial ingots of the Mg-10Gd (wt.%) were fabricated via sand casting. Prior to the deformation process, the initial alloy was treated at 530 °C for 10 h to homogenize the microstructure and mitigate the casting-related defects. The temperature and duration of homogenization are determined based on previous literature [42,43] and the phase diagram [44], which indicates that 530 °C and 10 h are sufficient to eliminate most of the casting defects. An extrusion-shearing process (ES) was then applied to the homogenized alloy at 400 °C. As shown in Fig. 1a, a direct extrusion (with ratio of 4) and 2 passes ECAP deformation with channel angle of 105° could be imposed through a single pass of ES deformation. During the hot deformation, the temperature of both the ingots and the die was maintained at 400 °C, and water-quenching treatment was immediately performed after the deformation. For comparison, Mg-10Gd ingots were also processed using a conventional direct extrusion process (EX) with an extrusion ratio of 13 under identical processing conditions (Fig. 1b). The applied von-Mises equivalent strains at the center of the extruded bars were calculated as 2.56 for the EX process and 2.54 for the ES process [40]. An extrusion speed of 20 mm/s was consistently maintained across both methods. Therefore, the strain path remained the sole variable between these two processes. The samples produced through these two methods were designated as the ES sample and the EX sample, respectively.

For microstructure observation, optical microscopy (OM) and scanning electron microscopy (SEM) techniques were employed. The samples were mechanically polished to a mirror finish on the extrusion direction-nominal direction (ED-ND) plane, followed by etching in a solution of 4 % Nital. The precipitates were analyzed using an energy dispersive spectrometer (EDS) attached to the SEM and transmission electron microscopy (TEM). Additionally, electron backscatter diffraction (EBSD) was conducted on the ED-ND plane of the deformed samples using a ZEISS Gemini SEM 560 machine. To ensure high precision in EBSD analysis, a step size of 0.3 μm was adopted. The EBSD results were subsequently analyzed using the ATEX software [45]. Quasi-static tensile tests were conducted along the ED direction at a strain rate of 1.5×10^{-3}. The gauge dimensions of the dog-bone-shaped samples were 2 mm × 3 mm × 5.5 mm. However, due to the reduced diameter of 10 mm in the extruded bar following the ES process, it was not feasible to prepare tensile test samples along the ND. Therefore, quasi-static compression tests were utilized to characterize the anisotropy of the mechanical properties. For compression testing, rectangular samples with side lengths of 5 mm were prepared.

3. Results

3.1. Microstructures

The microstructure of the homogenized ingot is shown in Fig. 2a. It reveals a non-uniform grain size distribution. After heat treatment, smaller grains had a diameter of ~50 μm, while grain sizes of larger grains reached 300 μm. The average grain size of the initial alloy was calculated to be 154 μm. As observed by SEM in Fig. 2b, a large number of insoluble particles larger than 10 μm still existed at grain boundaries after homogenization treatment. Based on EDS analysis (shown in Fig. 2b) of particle 1 (P1) and particle 2 (P2), these particles were identified as Gd-rich particles.

Fig. 3 presents microstructures of the Mg-10Gd alloy processed by the EX and ES processes. Although the two processes could apply the

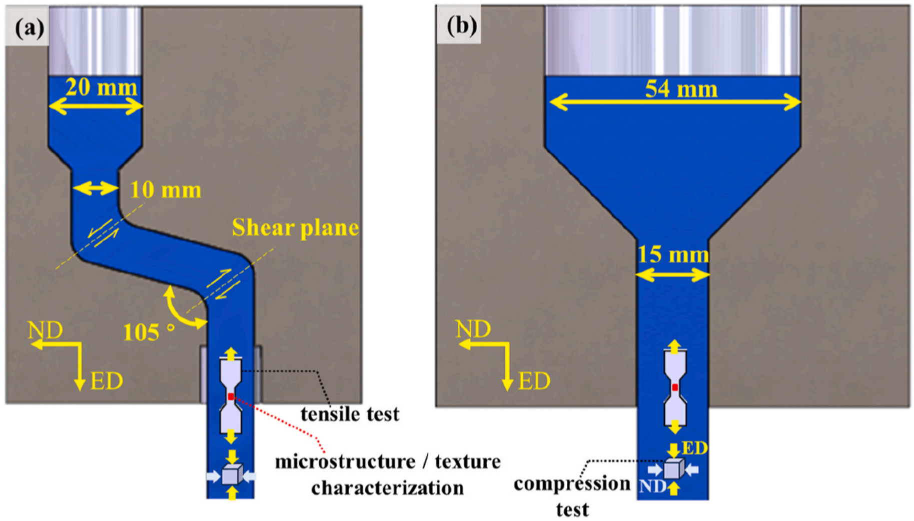

Fig. 1. Schematics of the deformation processes: (a) ES; (b) EX.

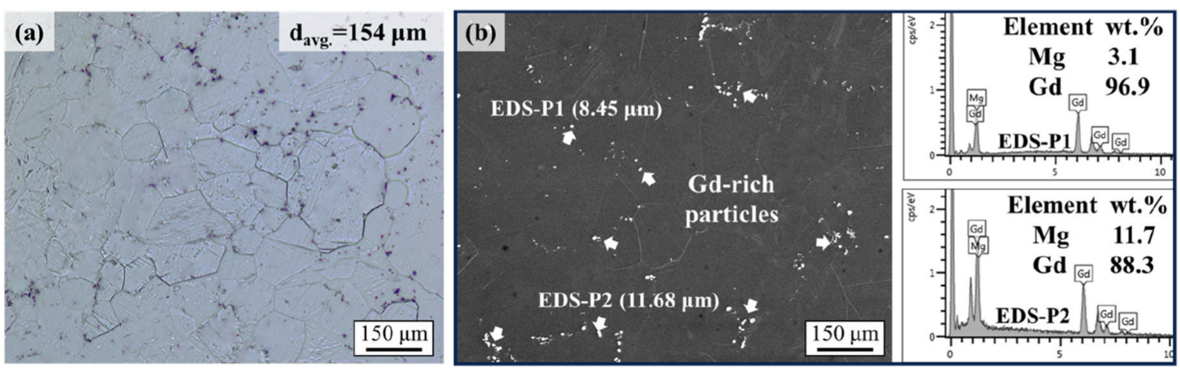

Fig. 2. Microstructure of initial homogenized Mg-10Gd alloy: (a) optical image; (b) SEM image with EDS-point analysis.

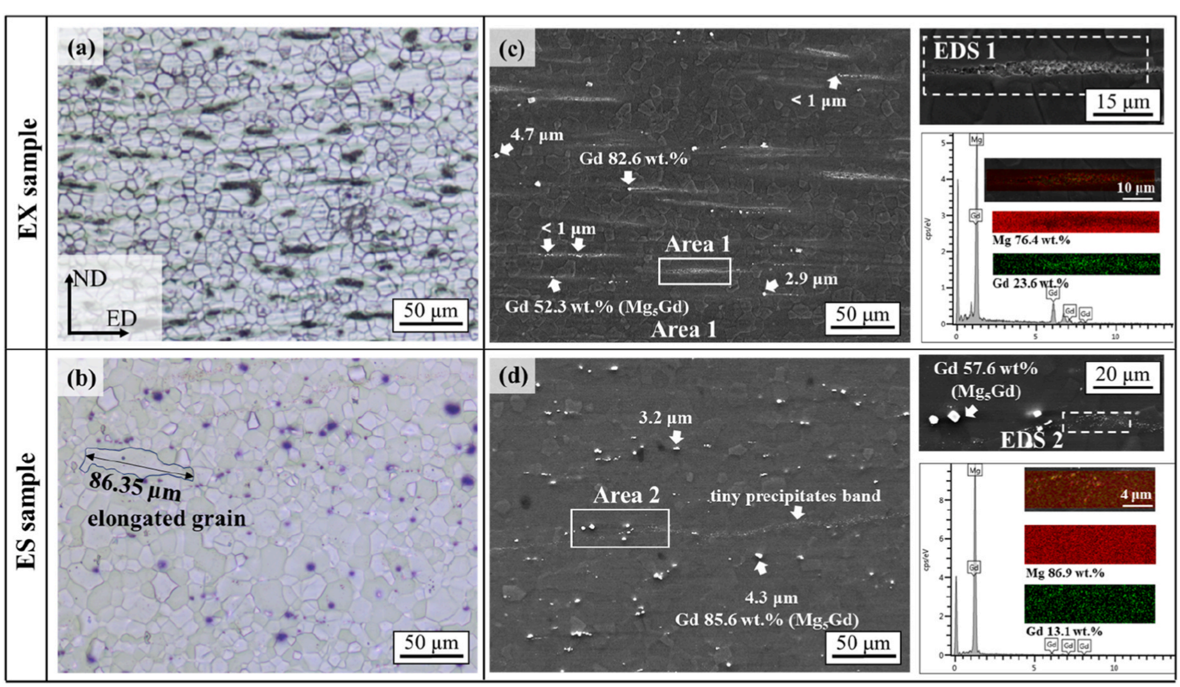

Fig. 3. Microstructure of Mg-10Gd alloy processed by EX and ES: (a–b) OM; (c–d) SEM images of deformed samples and quantitative analysis of elements in representative areas/points with EDS.

same von-Mises equivalent strain level, the deformed Mg-10Gd alloys exhibited distinctly different microstructures. In the EX sample, numerous deformation traces were formed parallel to ED (Fig. 3a and c). These deformation traces typically occur in rare-earth (RE) Mg alloys with high RE contents or after extrusion with a high ratio [46]. The traces occupy approximately 5 % of the area in the EX sample. Fig. 3c clearly indicates that a significant number of particles were present at the edges of or within the traces. Gd atoms were segregated in the traces, resulting in a Gd content of up to 23.6 wt% (Fig. 3c).

In the ES sample, the microstructure was significantly more uniform, without any observable deformation traces. As shown in Fig. 3b and d, the microstructure of ES sample is mainly composed of equiaxed grains, with elongated grains rarely observed. Some cuboidal and irregular particles were dispersed along grain boundaries in the ES sample. A large number of fine particles were distributed along the ED, forming a fine particle band. The EDS results show that the Gd content in these fine particles was higher than in the Mg matrix, indicating dynamic precipitation.

Furthermore, the Gd contents of the irregular and cuboid-shaped particles in the EX and ES samples were analyzed using EDS. The results indicate that the Gd contents in the irregular particles exceeded 80 wt%. These particles were refined during the hot deformation from the residual particles in the initial ingots. The cuboid-shaped particles are identified as the commonly observed Mg_5Gd precipitates in Mg–Gd alloys [47,48].

The composite strain paths resulting from extrusion and subsequent ECAP processing positively influenced the uniform refinement of the microstructure in the ES samples.

The EBSD Orientation Image Mappings (OIM) of the EX and ES samples are shown in Fig. 4. The related grain size distribution, dynamic recrystallization maps, and disorientation distributions are included. As seen in Fig. 4a, several ultrafine grains with grain sizes less than 1 μm appeared in the interior of the deformation traces of the EX sample. Thus, the deformation traces formed in the Mg-10Gd alloy after extrusion represent mixed regions of particles and ultrafine grains. This phenomenon aligns with the particle-stimulated nucleation (PSN) mechanism [49]. The average grain size of the EX sample is calculated to be 5.36 μm, with recrystallized grains accounting for 99.2 % and low-angle grain boundaries comprising 1.9 %.

When Mg-10Gd alloy is subjected to the ES process, elongated grains with specific orientations remain in the sample, as shown in Fig. 4d. In our previous study [40], it was demonstrated that these elongated grains were introduced by the upfront extrusion deformation with a small ratio during the ES process. The residual elongated grains tended to exhibit a typical basal orientation, where the <10-10> axis of the grains aligned with ED and the <0001> axis was oriented to ND. The average grain size of the ES sample was 4.74 μm. Following ES deformation, the Mg-10Gd alloy retained a high recrystallization ratio of 96.3 %. The EBSD results confirm that both the EX and ES processes achieved significant grain refinement.

3.2. From single-polar to multi-polar texture

Fig. 5 shows the micro-texture of the EX and ES samples with {0002}, {10-10} pole figures (PFs) and inverse pole figures (IPFs). The micro-texture calculation was based on the EBSD results in Fig. 4, accounting for more than 2500 grains. As shown in Fig. 5a–b, the EX sample exhibits a typical rare-earth texture (RE-texture) component with <2-1-12> || ED. The *c*-axis of the grains in the EX sample tended to rotate $\pm 10^\circ$–60° from ND to ED. The development of RE-texture is considered to be associated with RE atom segregation at grain boundaries [50,51], RE elements partitioning to dislocations [52], and the grain boundary pinning effect of precipitates [53]. However, the precise mechanism remains unclear at present.

Fig. 5d–f shows the texture of the ES sample, which differs significantly from that in the EX sample. After being processed via ES, shear texture components [34], such as B, P, Y, C_1 and C_2, are introduced into the Mg-10Gd alloy. The ideal shear texture components generated by ECAP were identified using the ATEX software, based on the defined die angle of 105°. As seen in Fig. 5e, the ideal shear texture components formed during the two-pass ECAP deformation in ES are marked, with the shear direction (SD1 and SD2) and the shear plane normal (SPN) indicated. The results demonstrate that the texture of the ES sample does not entirely conform to the ideal positions. In the ES sample, the B fiber displayed the highest texture intensity, and a weak C1 fiber texture was also observed. Interestingly, a novel texture component emerges, exhibiting a 22° clockwise rotation relative to C2. This new texture component develops along the shear direction, exhibiting an orientation of <2-1-12> || ED. Its intensity is surpassed only by that of the B fiber. Fig. 5f clearly shows that the angle between the *c*-axis of the grain and

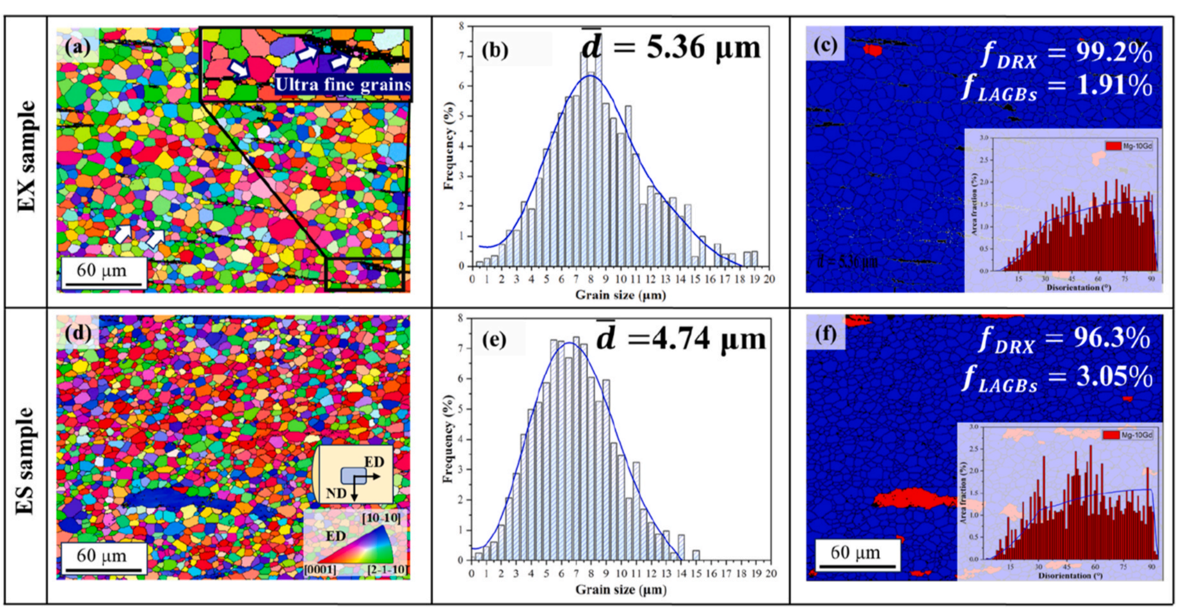

Fig. 4. Inverse pole figure (IPF) color maps of the microstructures, grain size distributions, recrystallization distributions (DRX grains in blue, deformed grains in red), and disorientation distributions: (a–c) EX sample, (d–f) ES sample.

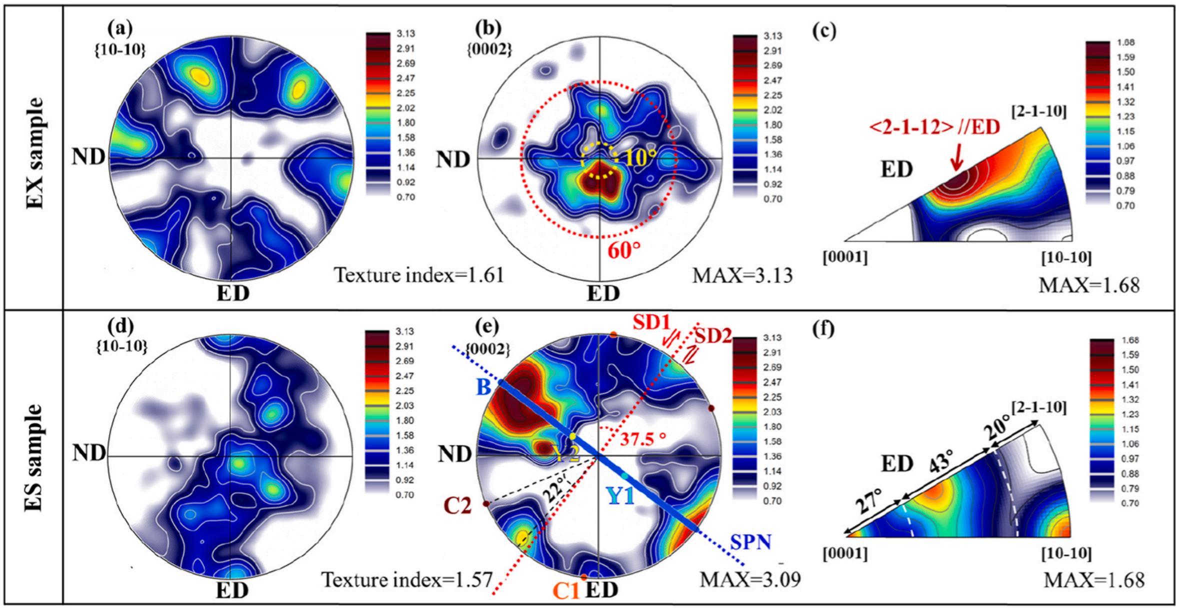

Fig. 5. Experimental textures on the ED-ND plane: (a, d) {10-10} and (b, e) {0002} pole figures and (c, f) ED inverse pole figures.

ED in the ES sample tends to cluster within three distinct ranges: 0–27°, 27°–70° and 70°–90°. The ES sample exhibits a distinct multipolar texture distribution.

3.3. Mechanical properties

The engineering strain-stress curves of the EX and ES samples under quasi-static tensile tests are presented in Fig. 6. The EX samples exhibited a tensile yield strength (TYS) of 138.82 MPa, ultimate tensile strength (UTS) of 223.74 MPa, and elongation to failure (EL) of 15.51 %. By contrast, the ES samples exhibited TYS of 166.48 MPa, UTS of 262.33 MPa, and EL of 23.33 %. Both strength and ductility were considerably enhanced compared to the EX samples.

Fig. 7a and c illustrate the true strain-stress curves of the EX and ES samples under compression, and the samples compressed along the ED and ND are designated as EX-ED, EX-ND, ES-ED and ES-ND, respectively. The compressive yield strength (CYS), ultimate compressive strength (UCS), and compression fracture strain (CEL) corresponding to each curve are listed in Table 1. Under uniaxial compression, the EX sample exhibits the lowest mechanical properties, with a CYS of 133.31 MPa and CEL of 0.22. Conversely, when the samples were subjected to compression along the ND, the ES sample demonstrateds superior strength and ductility, measured at 177.29 MPa and 0.27, respectively. In this study, the ratio of the CYS (CYS_{ED}/CYS_{ND}) was used to represent the anisotropy of the samples under compression. The experimental results indicate that the ratio of yield strength for the ES sample is 0.93, while for the EX sample, it is only 0.77.

In addition, the visco-plastic self-consistent (VPSC) modeling [54, 55] has been applied to capture the compression mechanical properties of the EX and ES sample. The procedure for the VPSC computational model refers to the latest VPSC code version 8 from the Los Alamos National Laboratory (open source). For uniaxial compression, the velocity gradients for the ED and ND loadings are as follows:

$$(\bar{\mathrm{L}})_{\mathrm{ED}} = \boldsymbol{L0}\begin{Bmatrix} -1 & 0 & 0 \\ 0 & 1/2 & 0 \\ 0 & 0 & 1/2 \end{Bmatrix} \tag{1}$$

$$(\bar{\mathrm{L}})_{\mathrm{ND}} = \boldsymbol{L0}\begin{Bmatrix} 1/2 & 0 & 0 \\ 0 & -1 & 0 \\ 0 & 0 & 1/2 \end{Bmatrix} \tag{2}$$

The orientation aggregate used in the VPSC simulation was calculated using the ATEX software based on the EBSD results shown in Figs. 4 and 5. In each aggregate, 5000 orientations were discretized and used to predict the compression performance. In VPSC modeling, the flow stress is calculated according to the Voce hardening law, which can be expressed as a function of the accumulated strain [56]:

$$\sigma(\varepsilon) = \sigma_0 + \sigma_1\left(1\text{-}\exp\left(\text{-}\frac{\theta_0\varepsilon}{\sigma_1}\right)\right) \tag{3}$$

where the σ_0 represents the initial yield stress, θ_0 is the initial hardening rate, and the saturation stress is given by $\sigma_0 + \sigma_1$. Considering that the hardening of each grain varies from grain to grain, Tome et al. [55] proposed an empirical hardening law. This law determines the resolved shear stress in each slip system of a grain as a function of its accumulated crystallographic shear:

$$\tau(\Gamma) = \tau_0 + (\tau_1 + \theta_1\Gamma)\left(1\text{-}\exp\left(\text{-}\frac{\Gamma\theta_0}{\tau_1}\right)\right) \tag{4}$$

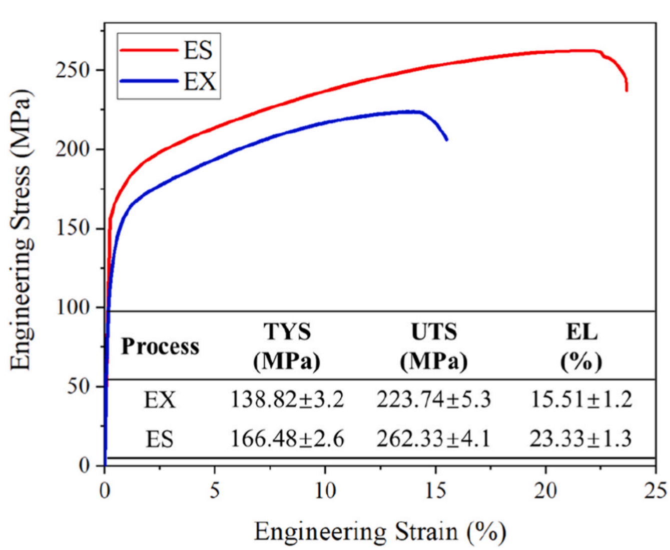

Process	TYS (MPa)	UTS (MPa)	EL (%)
EX	138.82±3.2	223.74±5.3	15.51±1.2
ES	166.48±2.6	262.33±4.1	23.33±1.3

Fig. 6. Mechanical properties of EX and ES samples under uniaxial tensile tests along extrusion direction.

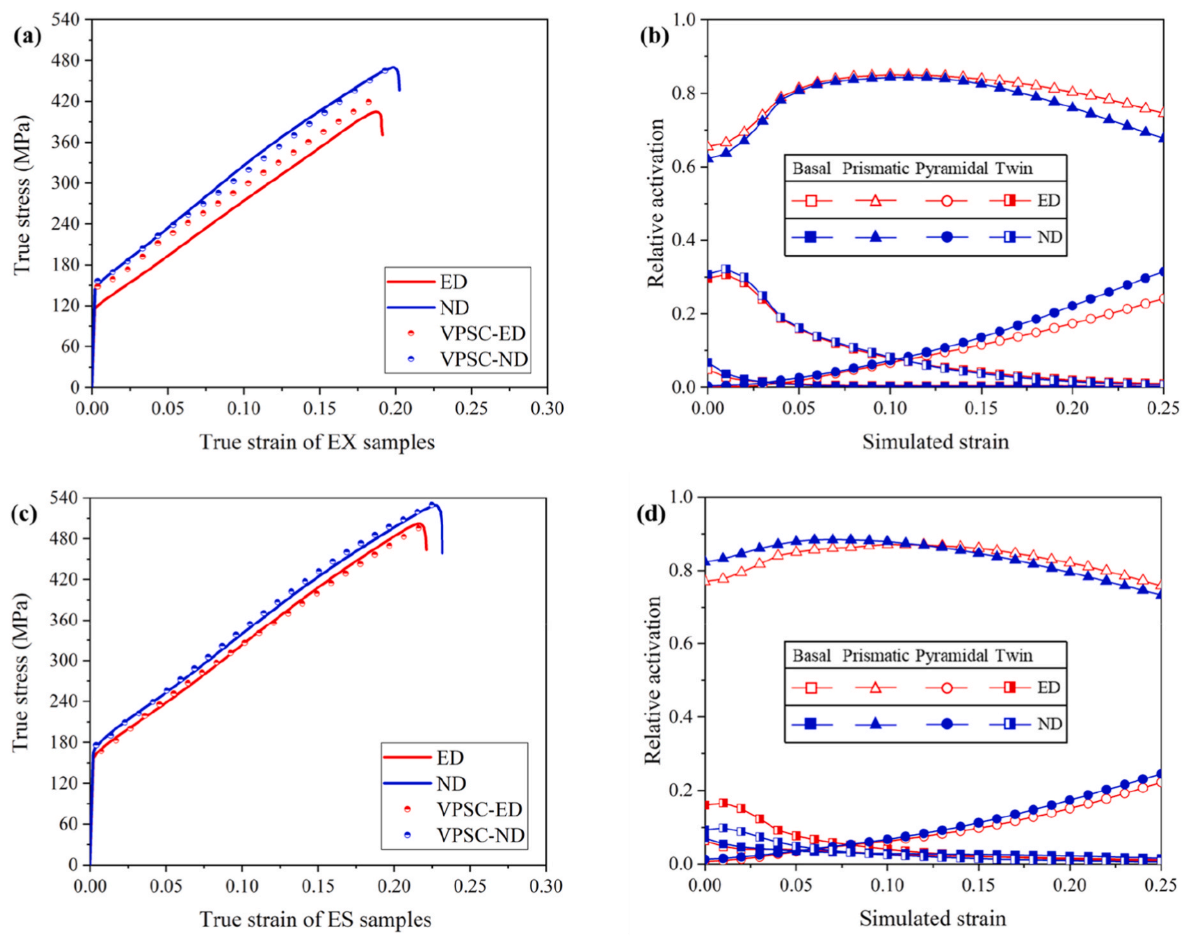

Fig. 7. (a, c) Experimental and simulated mechanical properties curves of EX and ES samples under uniaxial compression tests along extrusion direction and normal direction (b, d) relative activation of basal, prismatic, pyramidal sip and extension twining obtained by VPSC simulation.

Table 1
Mechanical properties statistics of the EX and ES samples under compression and related anisotropy ratio.

Process-Loading direction	CYS (MPa)	UCS (MPa)	CEL	CYS_{ED}/ CYS_{ND}
EX-ED	120.31 ± 8.2	404.72 ± 6.9	0.22 ± 0.03	0.77 ± 0.04
EX-ND	155.63 ± 5.6	487.37 ± 7.8	0.23 ± 0.03	
ES-ED	165.02 ± 4.3	502.23 ± 6.7	0.26 ± 0.01	0.93 ± 0.01
ES-ND	177.29 ± 2.5	528.47 ± 3.9	0.27 ± 0.02	

where τ_0 and θ_0 are the initial yield stress and hardening rate in the given slip system, and τ_1 and θ_1 determine the asymptotic hardening rate.

In recent years, VPSC modeling has been widely employed to predict the deformation mechanisms for Mg alloys. During the simulation of uniaxial compression, the influences of basal <a>, prismatic <a>, pyramidal <c+a> slip systems and {10–12} extension twinning on mechanical properties are typically considered. The activation of the deformation modes depends on the parameters τ_0, τ_1, θ_0, and θ_1. In previous studies, VPSC simulations have been extensively applied to analyze the deformation mechanisms of pure Mg [57], AZ31 [58], Mg-15Gd [57] alloys, and Mg-Gd-Y series alloys [59]. Adjusting the hardening parameters in VPSC modeling is a common method for obtaining well-fitted mechanical property curves. Based on previously reported hardening parameters for Mg-Gd-based alloys [43,45], Table 2 lists the adjusted hardening parameters used in this study, which were fitted by comparing the VPSC simulated curves with experimental curves in Fig. 7.

The simulated strain-stress curves are also presented in Fig. 7, and the simulated yield strength and anisotropy ratio are summarized in Table 3. The simulation results show that the simulated mechanical properties of the samples are basically consistent with the experimental results, except for the EX-ED sample. Unexpectedly, the simulated anisotropy ratio of the EX sample is 0.95, significantly higher than the experimental value of 0.77. This discrepancy will be discussed in Section 4. Fig. 7b–d shows the relative activation of the slip systems and <10-12> twinning in the EX and ES samples under the compression. Statistical results indicate that prismatic slip is the most activated mechanism in both the EX and ES samples. At the initial stage of compression deformation, the likelihood of twinning activation in the EX sample slightly exceeds that of the ES sample. The relative activation of the other deformation mechanisms and their trends are similar.

Table 2
Hardening parameters of VPSC modeling (unit is MPa).

Deformation mode	τ_0	τ_1	θ_0	θ_1
Basal <a>	35	110	100	80
Prismatic <a>	90	130	600	90
Pyramidal <c+a>	115	175	700	45
Extension twinning	60	80	60	40

Table 3
Simulated yield stress and yield anisotropy.

Process-Loading direction	Simulated yield stress (S_y, MPa)	Simulated yield anisotropy
EX-ED	148.36	0.95
EX-ND	156.40	
ES-ED	166.92	0.97
ES-ND	171.95	

4. Discussion

4.1. Specification of multi-polarization texture

To accurately characterize the differences in texture proportion in the Mg-10Gd alloy after conventional extrusion and the novel extrusion-shearing process, the angle distributions between the c-axis of the grains in the EX and ES samples and the ED were statistically analyzed and depicted in Fig. 8. This analysis aids in the classification and quantitative assessment of texture components. According to the IPF in Fig. 5f for the ES sample, grains with angles between the c-axis and the ED (θ) of 0°–27°, 27°–70°, and 70°–90° were separated from the related EBSD mapping and reproduced in the I-VI region of Figs. 8 and 9. The corresponding PFs and IPFs were also reconstructed and presented.

From Fig. 8, it is observed that the C-texture grains, which have their c-axis oriented along the ED, account for only 4.66 vol percent in the EX sample. As a result, when plotting the overall texture of the EX sample, the relative intensity of the C-texture is diminished by other components, rendering it unclear in the PF. In the EX sample, when the value of θ is within 27°–70° with respect to the ED, a RE-texture dominated by < 2-1-12> || ED forms, with a volume fraction of 51.32 % in the tested region. In region III, the grain colors are distinctly divided into blue and green. From the {0002} and {10-10} PFs corresponding to these grains, it is evident that these grains contribute to promoting the formation of an extrusion fiber texture in the Mg-10Gd alloy. These grains in region III can be further classified into two orientation types in the IPF: <2-1-10> || ED or <10-10> || ED.

Influenced by the composite strain path of the ES process, the Mg-10Gd alloy was first processed by a conventional extrusion deformation with a ratio of 4. As reported in our previous study [40], after extruded with ratio 4 at the first deformation stage, the main texture component is the extrusion fiber texture with <10-10> || ED. Subsequently, during the two ECAP deformation passes, dynamic recrystallization and grain rotation occur, forming grains with shear-induced orientations. Fig. 9 shows the texture composition of the ES sample. The area fractions corresponding to regions IV, V, and VI are 14.09 %, 57.95 %, and 27.96 %, respectively.

In the ES sample, the C-texture (regions IV) is significantly enhanced. Region V exhibits a typical bipolar texture distribution, not similar to region III of the EX sample. The distinction lies in the grains within region V: the grains in the {0002} PF display atwo single orientations, one indicating that the c-axis of these grains is parallel to the shear direction of the ECAP deformation zone. The other notable texture component in region V is the B fiber texture, which forms during ECAP processing and aligns the c-axis of the grains perpendicular to the shear plane.

From the IPF corresponding to region VI, it can be seen that in the ES sample, grains with θ > 70° are divided into two categories: <2-1-10> || ED and <10-10> || ED. The c-axis of these grains deviates from the ND (normal direction) by about 10°. Furthermore, grains with the <10-10> || ED orientation have a higher proportion. The ES sample exhibits smaller area fraction differences among grain orientations than the EX sample. Simultaneously, for the various grain types in the ES sample, the alignment of their c-axis demonstrates a tendency towards several specific directions, highlighting a trend of texture multi-polarization.

4.2. Strength and ductility

The strengthening and toughening of Mg alloys is primarily achieved through grain refinement, texture weakening, and precipitation controlling [4]. In this work, the average grain size of the homogenized Mg-10Gd alloy was refined from approximately 154 μm to around 5 μm after processing through both EX and ES deformation. Notably, the average grain size of the EX sample was slightly larger than that of the ES sample by only 0.67 μm. The texture index of the EX and ES samples were measured as 1.61 and 1.57 (Fig. 5), respectively, revealing a minor difference. However, the strength and elongation to failure of the ES samples significantly exceeded those of the EX samples.

In fact, the grain size distribution and microstructure morphology of the EX and ES samples exhibit clear differences. From the grain size distributions in Fig. 4b and e, we find that the percentage of grains larger than 10 μm in the EX sample is 32.65 %, which is 2.2 times higher than that in the ES sample (14.91 %). According to the Hall-Petch relationship (using a slope of k = 285 MPa [60]), the contribution of 10 μm grains to the yield strength in the Mg-10Gd alloy is calculated as 37.3 MPa less than that of 5 μm grains. This suggests that the presence of numerous large grains in the EX sample limits its strength improvement. In order to better understand the effect of precipitates, TEM was used to characterize the distribution of precipitates, and the results are presented in Fig. 11. It is obvious that the distribution of precipitates in the EX sample is more concentrated. The large-sized particles (1–2 μm) and fine particles (0.5–1 μm) are distributed in a line shape along the ED, and they tend to approach the extrusion traces or be within the trace (Fig. 3b). For the ES sample, as shown in Fig. 11c, numerous nano-precipitates (<200 nm) are formed with a dispersive distribution, which are rarely observed in the EX sample. Cuboid-shaped large particles prefer to be located at grain boundaries (Figs. 3c and 11d). Those nano-precipitates and cuboid-shaped precipitates will have a significant strengthening effect through the Orowan dislocation bypassing mechanism [61,62]. Therefore, the more abundant precipitation and its dispersive distribution can be another reason for the high strength of ES sample.

Additionally, by characterizing the microstructure of the EX sample after tensile tests (Fig. 11a), it is evident that the extrusion traces formed in the EX sample become nucleation sites for cracks during tension, significantly reducing the strength and ductility of the alloy. In contrast, due to the introduction of two passes of ECAP, the ES sample demonstrates a more uniform microstructure distribution, with stress being uniformly distributed during tension. This uniformity prevents the formation of cracks.

As for the precipitates in the ES sample, as shown in Fig. 11b, the cubic particles (Mg_5Gd) located along grain boundaries are fractured from the center after tension. This suggests that these precipitates contribute to enhancing the strength of the sample. Notably, there is no similar phenomenon observed in the EX sample.

In summary, the uniform and fine-grained microstructure achieved in the ES sample under the composite strain path of extrusion and ECAP process stands out as the main reason for its excellent tensile properties.

The microstructure of the EX and ES samples after compression tests is shown in Fig. 12. When the EX sample is compressed along the ED, the deformation traces become flattened. Comparing Figs. 3c to 12a, the length of the deformation traces reduces from 50 μm to 20 μm. In Fig. 12a, microvoids preferentially form within the deformation traces in the EX sample, which likely explains the lower experimental yield stress compared to the stress predicted by VPSC simulations.

Conversely, when compressed along the ND, the cross-section of deformation traces takes an ellipsoidal shape and becomes more uniformly distributed among the grains, thereby reducing mechanical property degradation during compression compared to compression along ED.

For ES samples, Fig. 12c–d indicates that the grains uniformly deform after compression along both the ED and ND. Moreover, no

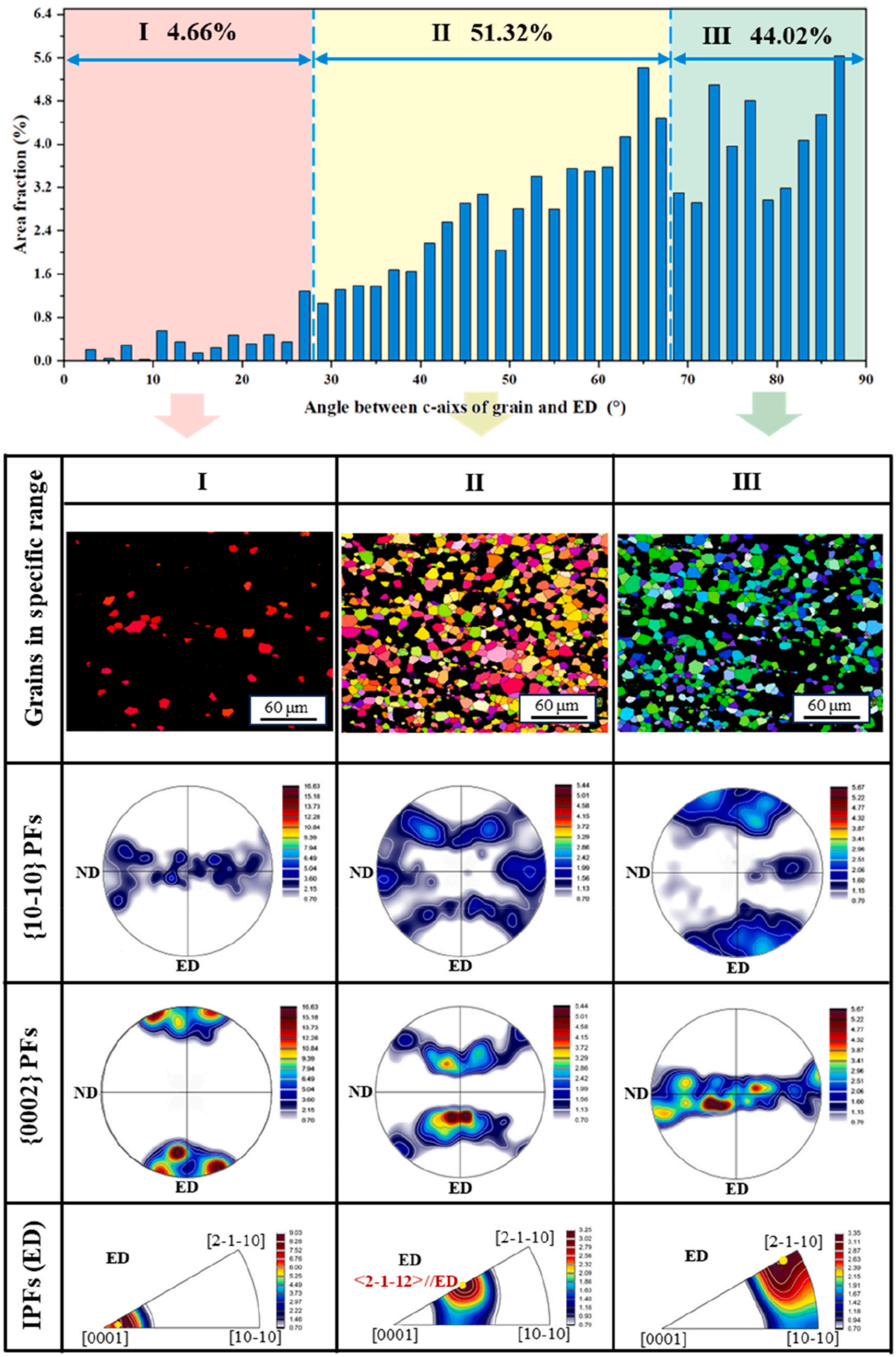

Fig. 8. Area fraction and texture contribution of grains with different angles between the c-axis of the grain and ED: EX sample.

microvoids are visible in the ES samples. Furthermore, the deformation twins are consistently concentrated within individual grains in both EX and ES samples. This observation might relate to the specific orientation of these grains.

The average Schmid factor value of basal slip, non-basal slip, and tensile twinning is displayed in Fig. 13 under compression condition. Based on the results, it can be inferred that the RE-texture formed in the EX sample and the multipolar texture distribution formed in the ES sample favor the initiation of the non-basal slip system. However, the texture composition differences of EX and ES samples are challenging to

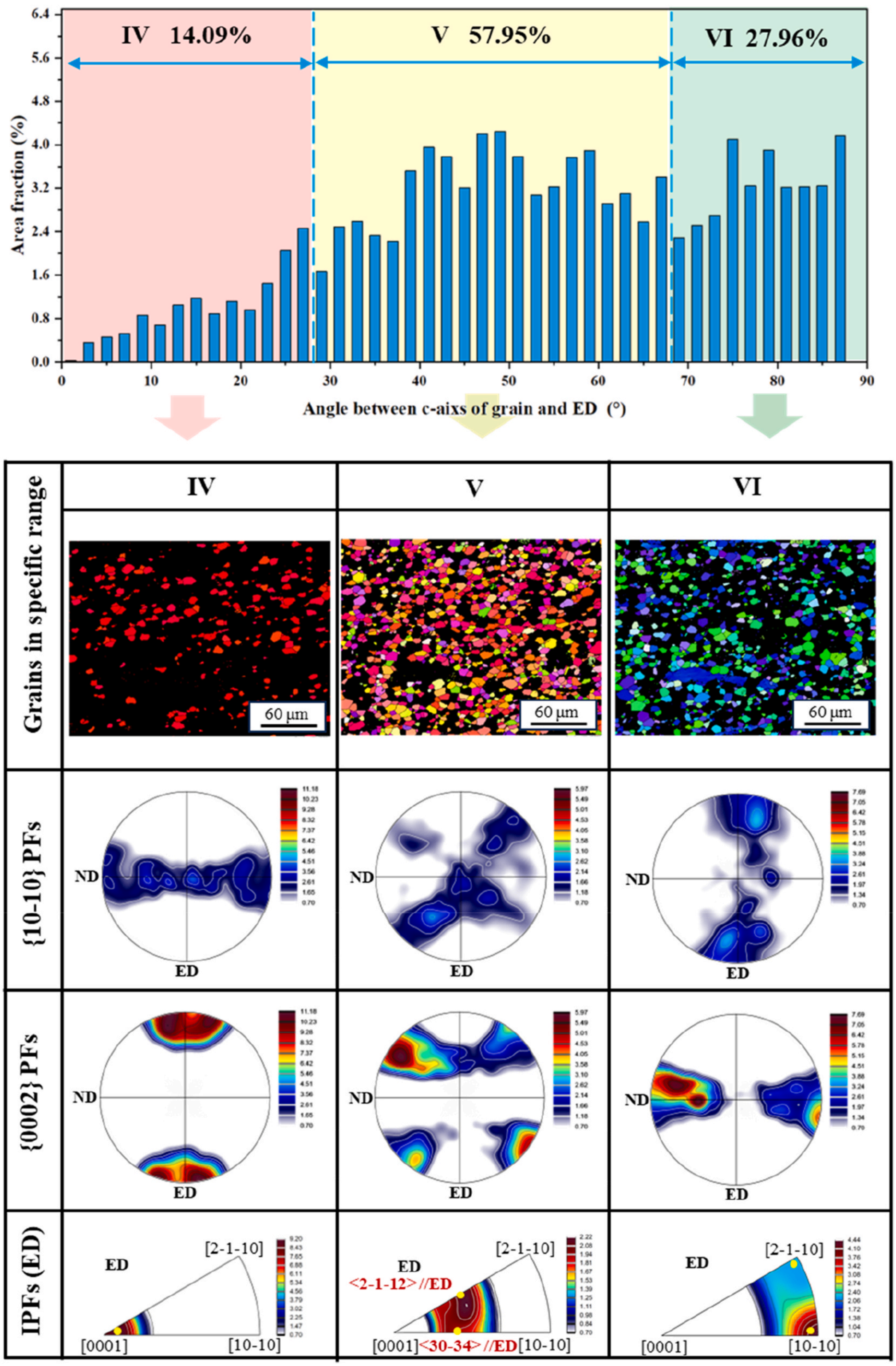

Fig. 9. Area fraction and texture contribution of grains with different angle between c-axis of grain and ED: ES sample.

discern by Schmid factor analysis.

4.3. Polycrystal plasticity simulation of anisotropy

In order to quantitatively analyze the effect of different texture components on the compression yield anisotropy of the EX and ES samples, the grain orientations corresponding to the main texture components in both samples were separated individually. By discretizing a single texture component from EX and ES samples into 5000 orientations, the ideal texture distributions were generated as shown in

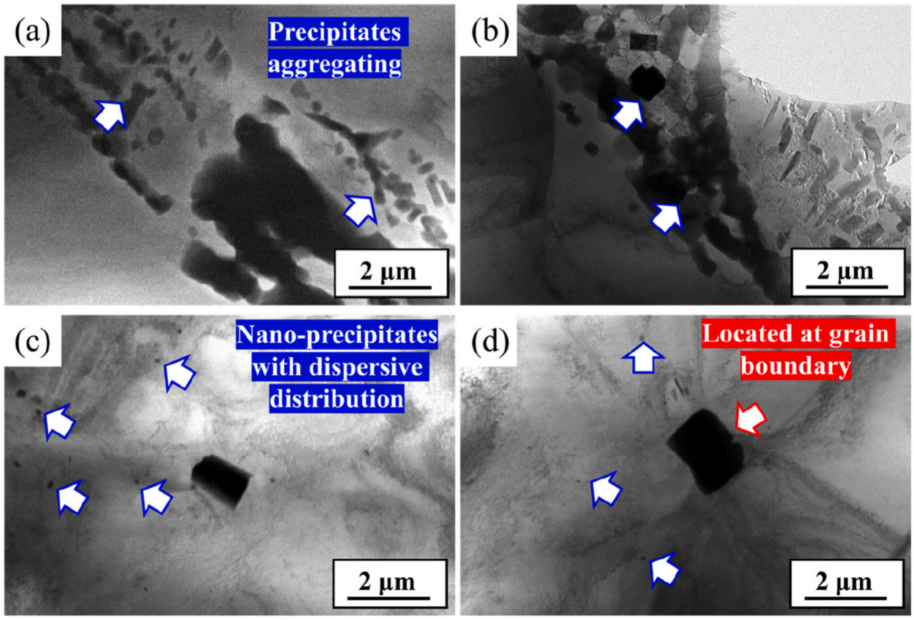

Fig. 10. Precipitates characterization with TEM: (a, b) EX sample; (c, d) ES sample.

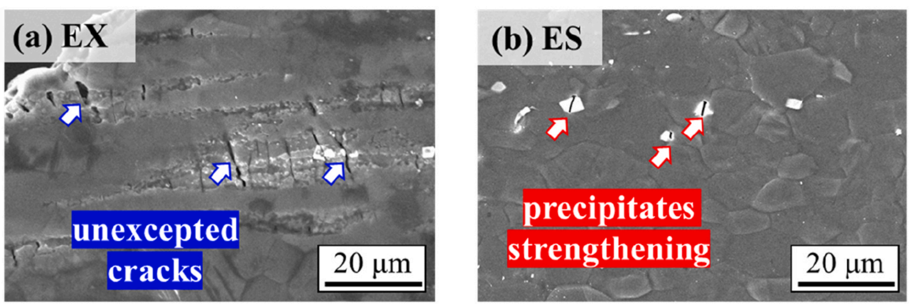

Fig. 11. Microstructure at crack edge of fractured samples under tension: (a) EX sample; (b) ES sample.

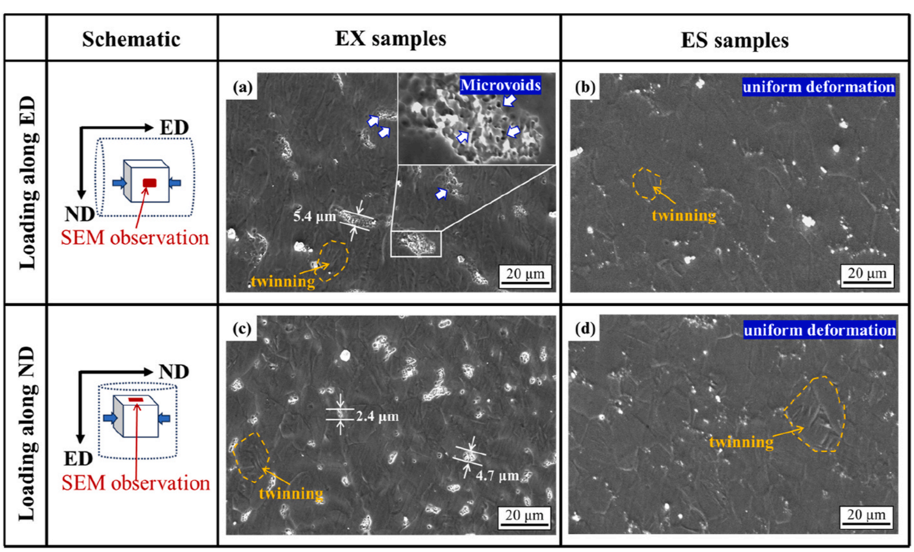

Fig. 12. Microstructure of fractured samples under compression: (a–b) EX samples; (c–d) ES samples.

Figs. 14 and 15. These texture components are labeled as T1-T8 and corresponding to: (1) RE-texture in the EX sample; (2) basal fiber texture with <2-1-10> || ED; (3) basal fiber texture with <10-10> || ED; (4) C-texture; (5) texture where the c-axis of grains tilts toward the shear direction; (6) B fiber texture; (7) texture with c-axis of grains tilted to ND and <2-1-10> || ED; (8) texture with c-axis of grains tilted to ND and

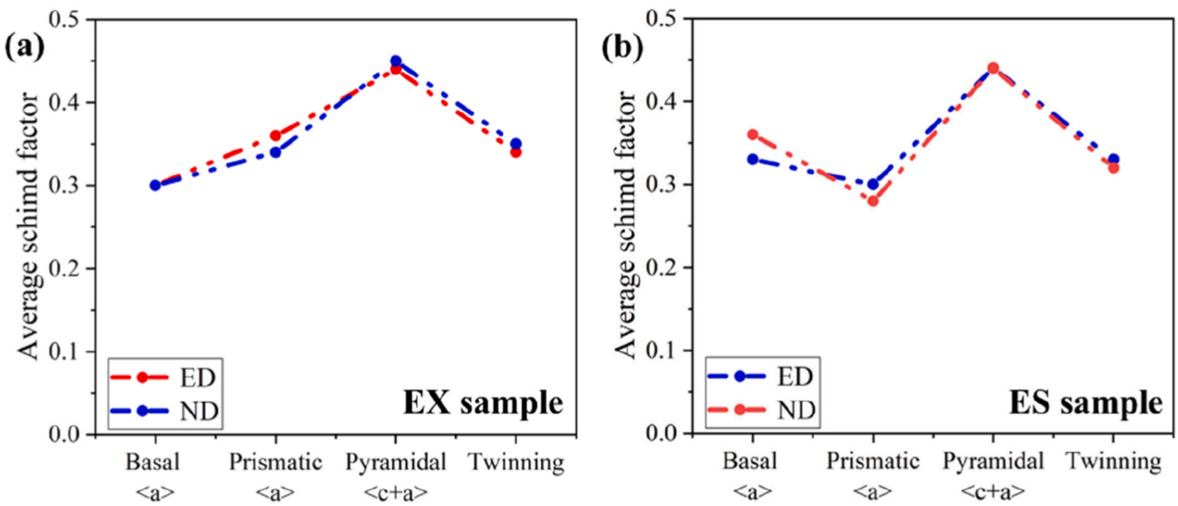

Fig. 13. Average Schmid factor of deformed samples under compression.

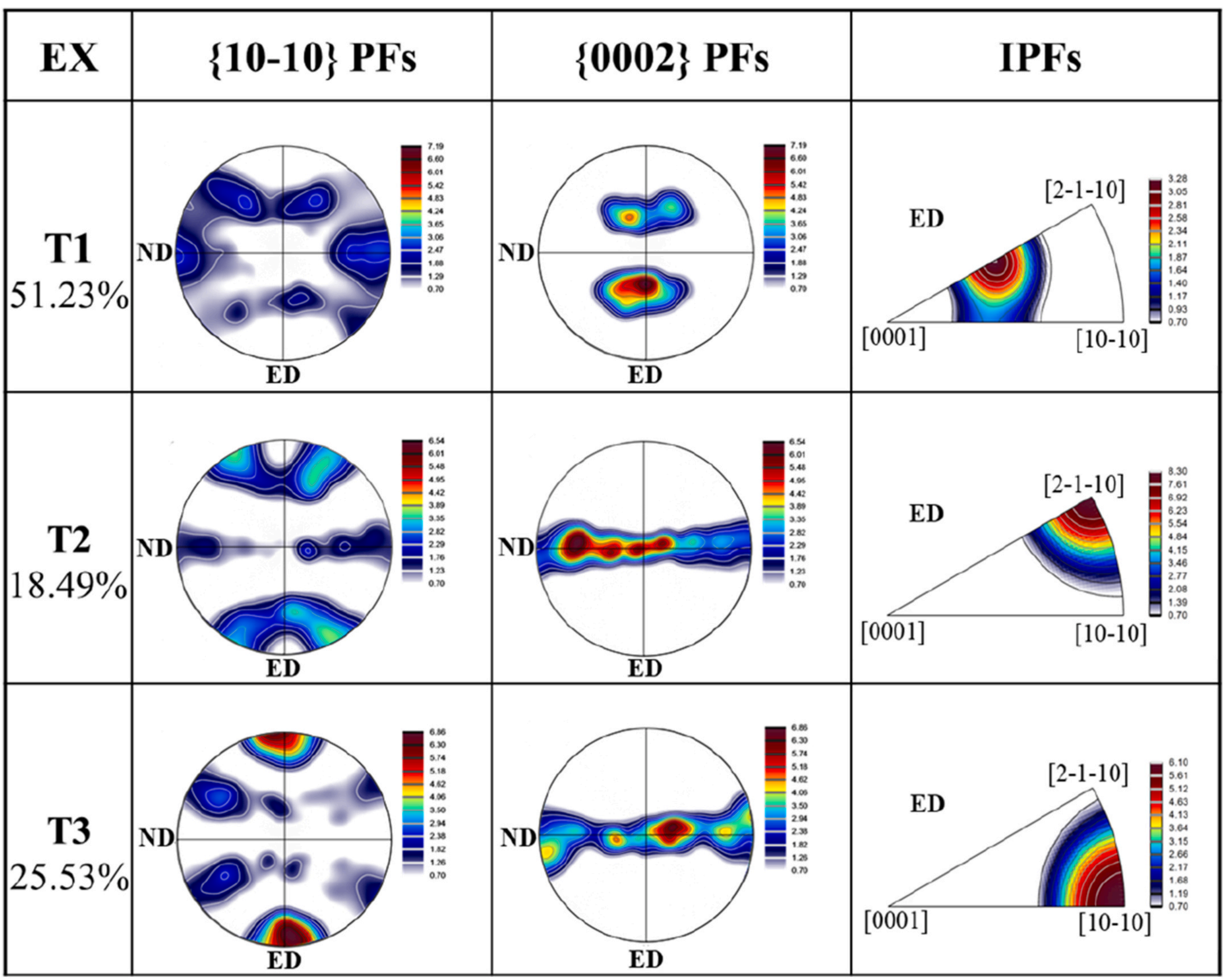

Fig. 14. Main texture components in EX sample with ideal distribution.

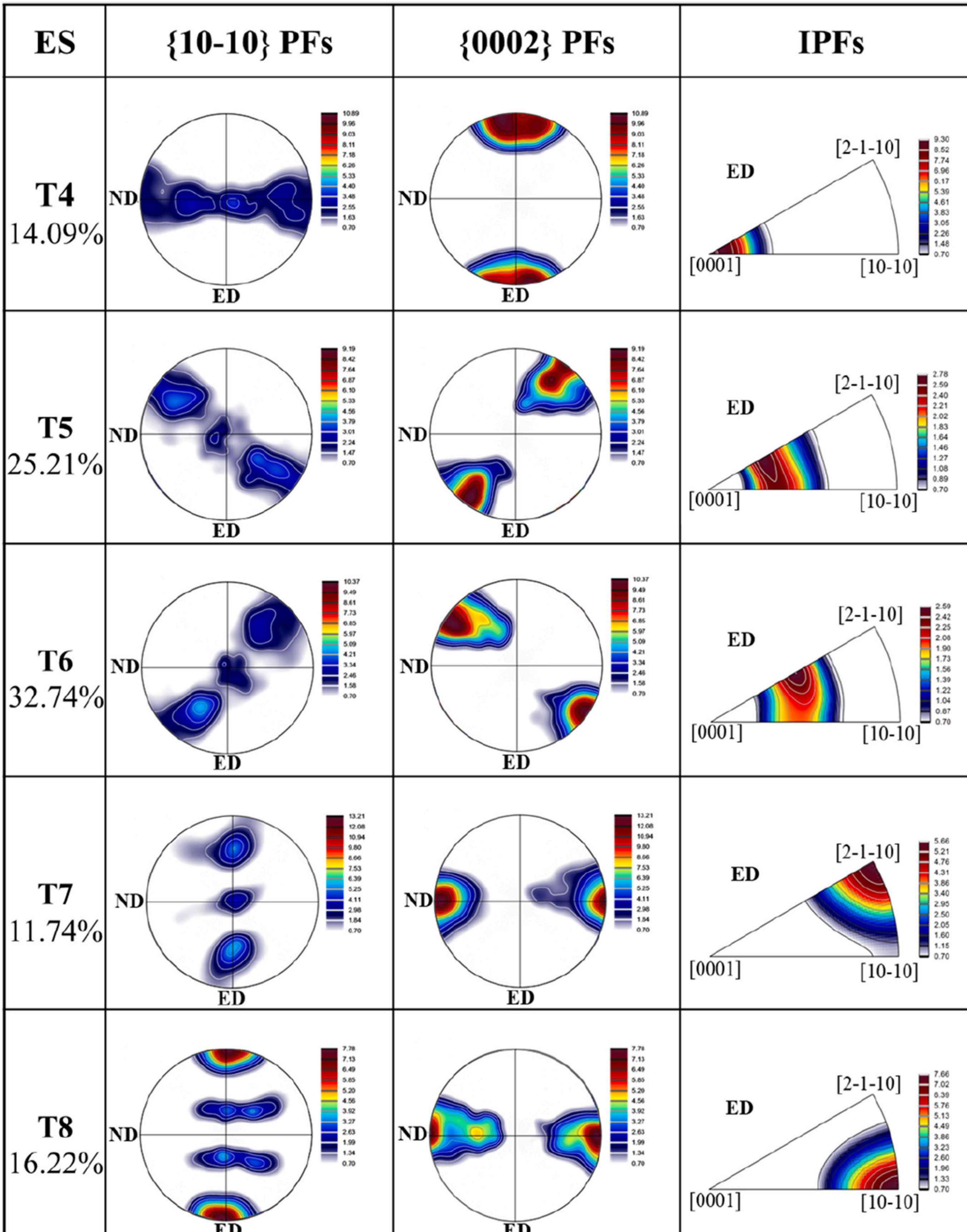

Fig. 15. Main texture components in ES sample with ideal distribution.

Table 4
Simulated yield stress and yield anisotropy of different texture components.

Process	Texture component	Simulated yield stress (S_y, MPa)		Ratio (ED/ND)
		ED	ND	
EX	T1	122.04	161.51	0.76
	T2	160.88	155.36	1.03
	T3	175.52	150.57	1.16
ES	T4	221.60	155.52	1.42
	T5	140.08	141.11	0.99
	T6	145.64	157.37	0.93
	T7	155.29	203.60	0.76
	T8	178.06	165.14	1.08

<10-10> || ED. The area fraction of grain related to those components are also marked in Figs. 14 and 15.

Table 4 summarizes yield strengths along the ED and ND for the eight texture components predicted through VPSC simulations, along with their ratio. It reveals that for textures T1 and T7, the yield strength under ED loading is significantly lower than ND loading, which is unfavorable for the anisotropy improvement in Mg-10Gd alloy. Conversely, textures T5 and T6 offer balanced contributions to the yield strength under both ED and ND loading, making them the most advantageous for improving the mechanical anisotropy of the alloy.

Of particular note is the texture T1(RE-texture), which has a yield strength of only 122.04 MPa when compressed along the ED, an aspect that limits its ability to enhance the yield strength of deformed Mg-10Gd alloy. In the EX sample, the good yield anisotropy observed in the VPSC simulations benefits from the promoting effect of basal textures T2-T3 on ED properties. However, during experimental tests, the mechanical performance of the ED sample significantly deteriorates under ED compression due to its non-uniform microstructure.

For the ES sample, the opposing impacts of textures T4 and T7 on anisotropy, along with their lower proportion of associated grains, are counterbalanced by the weak anisotropy of other components. This enables the ES sample to maintain high mechanical performance along both ED and ND directions.

Fig. 16 depicts the relative activation of slip systems and {10-12} twinning corresponding to textures T1-T3 in the EX sample, under ED and ND compression. As illustrated in Fig. 16a, the RE-texture T1 exhibits a higher tendency to activate prismatic slip across various compression processes. At the early stage of plastic deformation under ND compression T1 grains are more likely to activate twinning, while its activation probability under ED loading remains minimal. In contrast, the twinning activation behavior in T2-T3 textures follows an opposite trend compared to T1.

In the ES sample, as depicted in Fig. 17a, the C-texture initially exhibits a strong tendency to activate numerous twins under ND compression during the early stages of plastic deformation. As strain accumulates, the activation of non-basal slip systems progressively

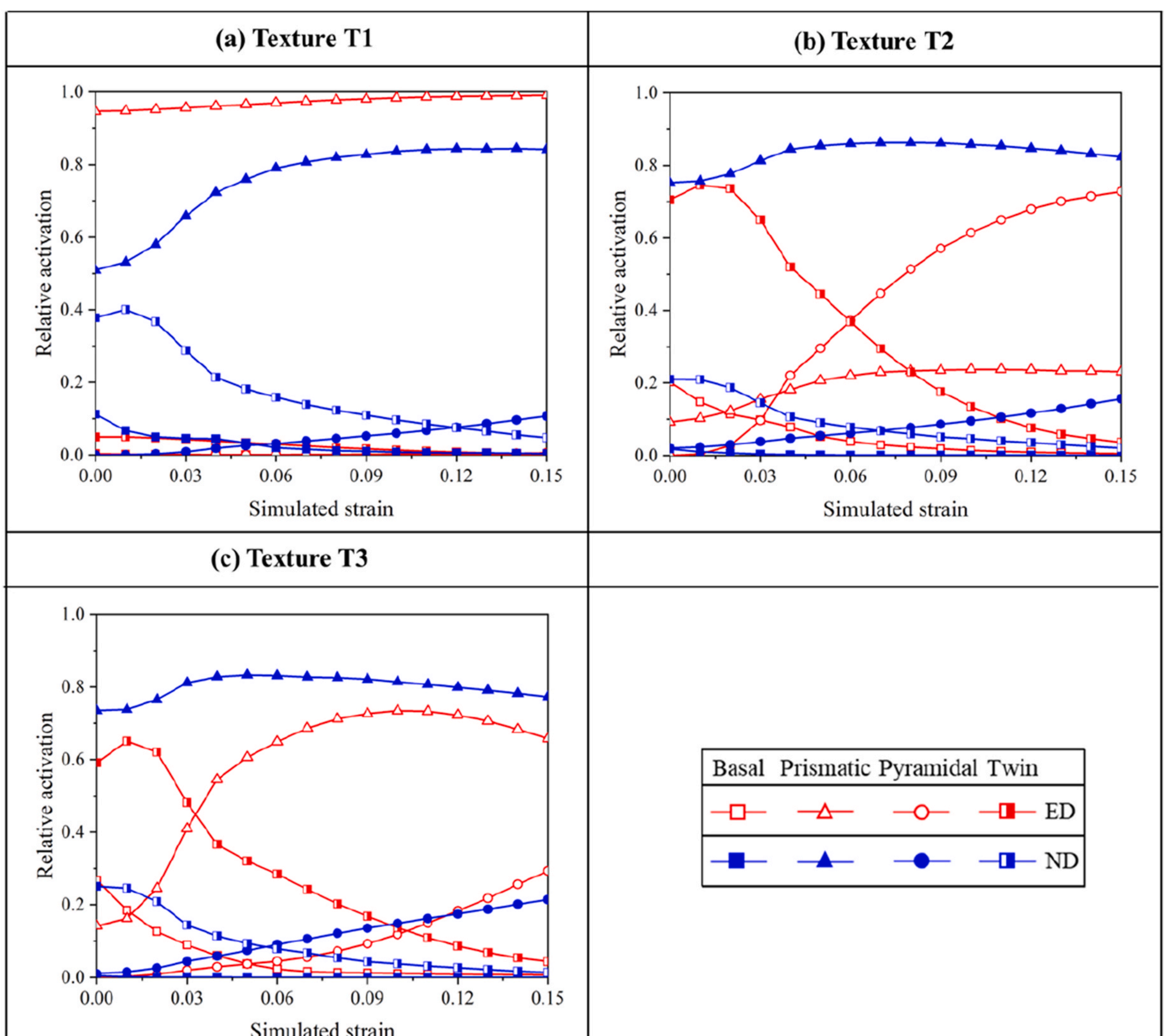

Fig. 16. Relative activation of basal, prismatic, pyramidal slip and extension twinning under compression of different texture components in EX sample.

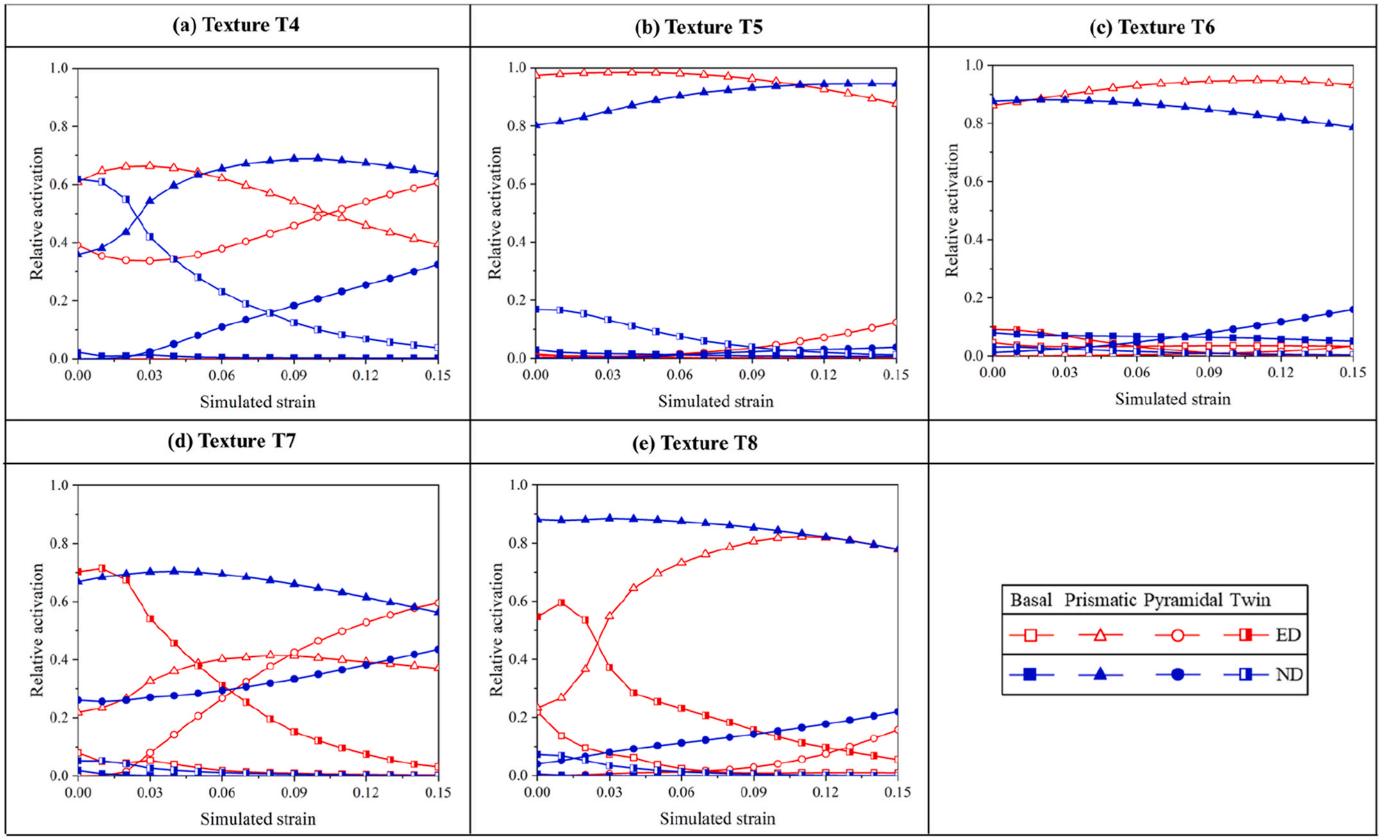

Fig. 17. Relative activation of basal, prismatic, pyramidal slip and extension twinning under compression of different texture components in ES sample.

increases. For textures T5-T6, the likelihood of twinning activation remains low under both ED and ND compression, with prismatic slip predominating during deformation.

For textures T7-T8, twin activation probability reaches approximatively 0.6 under ED compression but stays below 0.1 under ND compression. The statistical analysis in Figs. 16 and 17 underscores the pivotal role of anisotropy in twinning activation under loading along ED and ND, which significantly impacts yield stress and mechanical anisotropy.

5. Conclusion

In this study, the texture of Mg-10Gd alloy was effectively transformed into multi-polarized configuration by the extrusion shearing process (ES). The microstructure, texture evolution, and mechanical properties of ES sample were analyzed and compared to those of the conventionally extruded sample (EX). Compression anisotropy in both alloys was experimentally evaluated, and the influence of texture on deformation mechanisms was examined using visco-plastic self-consistent (VPSC) modeling under compression. The main conclusions are as follows.

1. Both EX and ES processes are capable of producing fine-grain Mg-10Gd alloys with an average grain size of approximatively 5 μm. However, under identical strain level, the ES-processed sample shown a synergistic enhancement in strength and plasticity, achieving TYS, UTS and TEL values of 166.48 MPa, 262.33 MPa and 23.33 %, respectively.
2. The EX process results in an uneven microstructure characterized by deformation traces. A basal RE-texture dominated by $<$ 2-1-12$>$ || ED was formed in the EX sample. Following the ES deformation, a uniform microstructure and multi-pole texture were achieved, benefiting the alloy's mechanical properties.
3. VPSC simulation revealed that the primary cause of anisotropy in the deformed Mg–Gd alloy is the difference in twinning activation under compression along different directions. The superior compression anisotropy ($CYS_{ED}/CYS_{ND} = 0.93$) of the ES sample is attributed to the multi-polarization of texture. Grains with the c-axis aligned with the shear direction (SD) and those with the c-axis oriented toward the shear plane normal (SPN) are the most favorable orientations.

Author contribution

Dongsheng HAN have contributed writing—original draft, validation, data curation, and investigation; Cai CHEN was responsible for funding acquisition, project administration, supervision, and writing—review and editing; Benoit BEAUSIR assisted in data curation and formal analysis; Zhonghua DU contributed to project administration, formal analysis and supervision; Sen YANG provided the experimental resources and assisted in writing—review and editing; Mingchuan Wang contributed to formal analysis and writing—review and editing; Rui REN assisted in data curation; Fengjian SHI contributed to experimental resources and formal analysis; Yuli ZHOU contributed to experimental resources and formal analysis; Wei CHEN contributed to project administration, formal analysis and supervision; Werner SKROTZKI assisted in writing—review and editing; Zhangzhi SHI was responsible for funding acquisition, project administration, and supervision; Laszlo S TOTH contributed to validation, project administration, formal analysis and supervision.

Data availability

All data included in this study are available upon request by contact with the corresponding author.

Declaration of competing interest

The authors declare that they have no known competing financial interests or personal relationships that could have appeared to influence the work reported in this paper.

Acknowledgements

The authors are grateful for the financial support provided by the National Natural Science Foundation of China (grant numbers 51901101 and 52271088). L.S. Toth was supported by the National Research, Development and Innovation Office, Hungary, under K143800 "New avenues of production of bulk and composite nano-structured metals; experiments, characterization, modelling" project.

References

[1] Song GL, Atrens A. Recently deepened insights regarding Mg corrosion and advanced engineering applications of Mg alloys. J Magnes Alloys 2023;11:3948–91.
[2] Jayasathyakawin S, Ravichandran M, Baskar N, Anand Chairman C, Balasundaram R. Mechanical properties and applications of magnesium alloy-review. Mater Today Proc 2020;27:909–13.
[3] Kumar A, Choudhari A, Gupta AK, Kumar A. Rare-Earth based magnesium alloys as a potential biomaterial for the future. J Magnes Alloys 2024;12(10):3841–97.
[4] Wang SQ, Zha M, Jia HL, Yang YJ, Wang DW, Wang C, et al. A review of superplastic magnesium alloys: focusing on alloying strategy, grain structure control and deformation mechanisms. J Mater Sci Technol 2025;211:303–19.
[5] Wei K, Hu R, Yin DD, Xiao LR, Pang S, Cao Y, et al. Grain size effect on tensile properties and slip systems of pure magnesium. Acta Mater 2021;206:11604.
[6] Zhang L, Yuan Q, Tan J, Dong Q, Lv H, Wang F, et al. Enhancing the room-temperature plasticity of magnesium alloys: mechanisms and strategies. J Magnes Alloys 2024;12(12):4741–67.
[7] Feng XY, Wang LF, Chen X, Deng KK, Wang X, Zheng LW, et al. Recent plastic technologies development of basal texture control to improve the property of wrought Mg alloys-a review. J Mater Res Technol 2025;34:1165–90.
[8] Xu C, Zheng MY, Xu SW, Wu K, Wang ED, Fan GH, et al. Microstructure and mechanical properties of Mg-Gd-Y-Zn-Zr alloy sheets processed by combined processes of extrusion, hot rolling and ageing. Mater Sci Eng A 2013;559:844–51.
[9] Zhao CY, Li ZY, Shi JH, Chen XH, Tu T, Luo Z, Cheng R, Atrens A, Pan FS. Strain hardening behavior of Mg-Y alloys after extrusion process. J Magnes Alloys 2019;7:672–80.
[10] Xu BQ, Sun JP, Yang ZQ, Xiao LR, Zhou H, Han J, et al. Microstructure and anisotropic mechanical behavior of the high-strength and ductility AZ91 Mg alloy processed by hot extrusion and multi-pass RD-ECAP. Mater Sci Eng A 2020;780:139191.
[11] Shi BD, Yang C, Peng Y, Zhang FC, Pan FS. Anisotropy of wrought magnesium alloys: a focused overview. J Magnes Alloys 2022;10(6):1476–510.
[12] Zhang ZM, Yu JM, Xue Y, Dong BB, Zhao X, Wang Q. Recent research and development on forming for large magnesium alloy components with high mechanical properties. J Magnes Alloys 2023;11:4054–81.
[13] Qi XX, Li YX, Xu XY, Liu YX, Zhang H, Zhu QC, et al. Enhancing strength–ductility synergy in a Mg-Gd-Y-Zr alloy at sub-zero temperatures via high dislocation density and shearable precipitates. J Mater Sci Technol 2023;166:123–32.
[14] Li DD, Le QC, Hu CL, Li XQ, Zhou X, Guo RZ, et al. The influence of initial texture, microstructure and deformation behavior on the low mechanical anisotropy of extruded Mg alloy tube. J Mater Res Technol 2020;20:3485–98.
[15] Zhao JQ, Guo HS, Luo TT, Zhang CX, Luo JT. Microstructure evolution and grain refinement mechanism of fine-grained Mg-Gd-Y-Zn-Zr alloy during multi-directional forging. J Alloys Compd 2022;928:167199.
[16] Straumal BB, Kulagin R, Klinger L, Rabkin E, Straumal PB, Kogtenkova OA, et al. Structure refinement and fragmentation of precipitates under severe plastic deformation: a review. Mater 2022;15:601.
[17] Lin JB, Wang XY, Ren WJ, Yang XX, Wang QD. Enhanced strength and ductility due to microstructure refinement and texture weakening of the GW102K alloy by cyclic extrusion compression. J Mater Sci Technol 2016;32:783–9.
[18] Lin JB, Ren WJ, Wang QD, Ma LF, Chen YJ. Influence of grain size and texture on the yield strength of Mg alloys processed by severe plastic deformation. Adv Mater Sci Eng 2014;1:356572.
[19] Xu BQ, Sun JP, Yang ZQ, Han J, Fu YT, Jiang JH, et al. A near-isotropic ultrafine-grained Mg-Gd-Ag alloy with high strength-ductility synergy. J Mater Res Technol 2020;9:13616–24.
[20] Ren R, Fan JF, Wang BS, Zhang Q, Li WG, Dong HB. Hall-Petch relationship and deformation mechanism of pure Mg at room temperature. J Alloys Compd 2022;920:165924.
[21] Lin JB, Wang QD, Peng LM, Roven HJ. Microstructure and high tensile ductility of ZK60 magnesium alloy processed by cyclic extrusion and compression. J Alloys Compd 2009;476:441–5.
[22] Lin H, Huang JC, Langdon TG. Relationship between texture and low temperature superplasticity in an extruded AZ31 Mg alloy processed by ECAP. Mater Sci Eng A 2005;402:250–7.
[23] Hoseini-Athar MM, Mahmudi R, Prasath Babu R, Hedström P. Tailoring the texture of an extruded Mg sheet through constrained groove pressing for achieving low mechanical anisotropy and high yield strength. Scripta Mater 2020;186:253–8.
[24] Wu JL, Jin L, Dong J, Wang FH, Dong S. The texture and its optimization in magnesium alloy. J Mater Sci Technol 2020;42:175–89.
[25] Zhao LY, Xin YC, Wu Y, Liu Q. The texture dependence of strength in slip and twinning predominant deformations of Mg-3Al-1Zn alloy. Mater Sci Eng A 2018;717:34–40.
[26] Song B, Yang QS, Zhou T, Chai LJ, Guo N, Liu TT, et al. Texture control by {10-12} twinning to improve the formability of Mg alloys: a review. J Mater Sci Technol 2019;35:2269–82.
[27] Najafi S, Sabbaghian M, Sheikhani A, Nagy P, Fekete K, Gubicza J. Effect of addition of rare earth elements on the microstructure, texture, and mechanical properties of extruded ZK60 alloy. Metals Mater Int 2022;29:1699–711.
[28] Ma YJ, Liu CM, Jiang SD, Wan YC, Chen ZY. Microstructure, mechanical properties and damping capacity of as-extruded Mg-1.5Gd alloys containing rare-earth textures. Mater Charact 2022;189:111969.
[29] Li X, Liu C, Wang JS, Zhang C. Tailoring the strength and formability of Mg alloys through rare earth element additions (Gd and Dy) and dynamic recrystallizations. Mater Today Commun 2021;28:102627.
[30] Hidalgo-Manrique P, Robson JD, Pérez-Prado MT. Precipitation strengthening and reversed yield stress asymmetry in Mg alloys containing rare-earth elements: a quantitative study. Acta Mater 2017;124:456–67.
[31] Imandoust A, Barrett CD, Al-Samman T, Inal KA, El Kadiri HE. A review on the effect of rare-earth elements on texture evolution during processing of magnesium alloys. J Mater Sci 2016;52(1):1–29.
[32] Li N, Li YQ, Wang CY, Shi DF, Yang LW. Effect of dilute atom Gd on critical resolved shear stress and anisotropic deformation mechanism of Mg-Gd alloy. Mater Today Commun 2024;38:107630.
[33] Xu WL, Chen XH, Pan FS. Effect of Y content on the microstructure and mechanical anisotropy of Mg–6Zn-xY-0.5Ce-0.4Zr alloy subjected to asymmetric rolling. Mater Sci Eng A 2023;882:145465.
[34] Beausir B, Tóth LS, Neale KW. Ideal orientations and persistence characteristics of hexagonal close packed crystals in simple shear. Acta Mater 2007;55:2695–705.
[35] Zhao LY, Zhou BN, Zhu W, Yan CJ, Jin ZY, Guo XQ. A comprehensive study on the mechanical behavior, deformation mechanism and texture evolution of Mg alloys with multi texture components. J Alloys Compd 2022;907:164342.
[36] Zhao LY, Guan B, Xin YC, Huang XX, Liu CD, Wu PD, et al. A quantitative study on mechanical behavior of Mg alloys with bimodal texture components. Acta Mater 2021;214:117013.
[37] Liu S, Wang C, Ning H, Meng ZY, Guan K, Wang HY. Achieving high ductility and low in-plane anisotropy in magnesium alloy through a novel texture design strategy. J Magnes Alloys 2024;12(7):2863–73.
[38] Sun JP, Yang ZQ, Han J, Yuan T, Song D, Wu YN, et al. Enhanced quasi-isotropic ductility in bi-textured AZ91 Mg alloy processed by up-scaled RD-ECAP processing. J Alloys Compd 2019;780:443–51.
[39] Chen C, Han DS, Wang MC, Cai T, Liang NN, Beausir B, et al. The effect of rotary-die equal-channel angular pressing process on the microstructure, the mechanical and friction properties of GW103 alloy. Mater 2022;15:9005.
[40] Chen C, Han DS, Wang MC, Xu S, Cai T, Yang S, et al. High strength and high ductility of Mg-10Gd-3Y alloy achieved by a novel extrusion-shearing process. J Alloys Compd 2023;931:167498.
[41] Jiang X, Shi FJ, Lu QS, Wang JH, Guo JW, Chen TX, et al. High strength and high ductility combination of biodegradable high-purity magnesium fabricated by forward extrusion and extrusion-shear process. J Alloys Compd 2025;1026:180388.
[42] Vlcek M, Cizek J, Lukac F, Hruska P, Smola B, Stulikova I, et al. Hydrogen absorption in Mg-Gd alloy. Int J Hydrogen Energy 2017;42(35):22598–604.
[43] Hu XY, Peng LM, Qian SQ, Fu PH, Ding WJ. Effects of intermediate frequency magnetic field on the solution treatment of Mg–Gd alloy. Mater Lett 2014;123:238–41.
[44] Hampl M, Blawert C, Silva Campos MR, Hort N, Peng Q, Kainer KU, et al. Thermodynamic assessment and experimental study of Mg–Gd alloys. J Alloys Compd 2013;581:166–77.
[45] Fundenberger JJ, Beausir B. Analysis Tools for electron and X-ray diffraction. ATEX-software; 2017. www.atex-software.eu. Université de Lorraine - Metz.
[46] Xu C, Nakata T, Qiao XG, Jiang HS, Sun WT, Chi YC, et al. Effect of extrusion parameters on microstructure and mechanical properties of Mg-7.5Gd-2.5Y-3.5Zn-0.9Ca-0.4Zr (wt%) alloy. Mater Sci Eng A 2017;685:159–67.
[47] Bayat-Tork N, Saghafian H, Razavi SH, Al-Fadhalah KJ, Ebrahimi R, Mahmudi R. Microstructure and texture characterization of Mg–Al and Mg–Gd binary alloys processed by simple shear extrusion. J Mater Res Technol 2019;8:1288–99.
[48] Peng Q, Ma N, Li H. Gadolinium solubility and precipitate identification in Mg-Gd binary alloy. J Rare Earths 2012;30:1064–8.
[49] Li M, Shi ZZ, Wang Q, Cheng Y, Wang LN. Zn–0.8Mn alloy for degradable structural applications: hot compression behaviors, four dynamic recrystallization mechanisms, and better elevated-temperature strength. J Mater Sci Technol 2023;137:159–75.
[50] Jiang MG, Xu C, Yan H, Lu SH, Nakata T, Lao CS, et al. Correlation between dynamic recrystallization and formation of rare earth texture in a Mg-Zn-Gd magnesium alloy during extrusion. Sci Rep 2018;8:16800.

[51] Barrett DC, Imandoust A, Kadiri EH. The effect of rare earth element segregation on grain boundary energy and mobility in magnesium and ensuing texture weakening. Scripta Mater 2018;146:46–50.
[52] Stanford N. The effect of rare earth elements on the behaviour of magnesium-based alloys: Part 2-recrystallisation and texture development. Mater Sci Eng A 2013; 565:469–75.
[53] Hou XL, Zhai YX, Zhang P, Guo S, Yuan ZZ, Guan QF. Rare earth texture analysis of rectangular extruded Mg alloys and a comparison of different alloying adding ways. Rare Met 2016;35:850–7.
[54] Lebensohn RA, Tome CN. A self-consistent anisotropic approach for the simulation of plastic deformation and texture development of polycrystals: application to zirconium alloys. Acta Metall Mater 1993;41:2611–24.
[55] Tome CN, Canova GR, Kocks UF, Christodoulou N, Jonas JJ. The relation between macroscopic and microscopic strain hardening in F.C.C. polycrystals. Acta Metall 1984;32:1637–53.
[56] Tome CN, Lebensohn RA. Material modeling with the visco-plastic self-consistent (VPSC) approach: theory and practical applications. San Diego: Elsevier; 2023. p. 112.
[57] Xu Y, Huang Y, Wang Y, Gan W, Wang S, Maawad E, et al. Investigations on the tensile deformation of pure Mg and Mg–15Gd alloy by in-situ X-ray synchrotron radiation and visco-plastic self-consistent modeling. J Magnes Alloys 2023;11: 607–13.
[58] Yi SB, Davies CHJ, Brokmeier HG, Bolmaro RE, Kainer KU, Homeyer J. Deformation and texture evolution in AZ31 magnesium alloy during uniaxial loading. Acta Mater 2006;54:549–62.
[59] Zhang XH, Zhou R, Li C, Guo SM, Yue HY. A visco-plastic self-consistent analysis of the compression anisotropy in extruded rare earth magnesium alloy. J Mater Res Technol 2024;29:2154–65.
[60] Wen Y, Guan B, Xin YC, Liu CL, Wu PL, Huang GJ, et al. Solute atom mediated Hall-Petch relations for magnesium binary alloys. Scripta Mater 2020;210:114451.
[61] Shao X, Tan ZD, Xia L, Guo YL, Li SX, Sha SM, et al. Theoretical investigation on aging precipitation mechanisms and precipitation strengthening effect of Mg-Gd alloy. J Solid State Chem 2025;346:125285.
[62] Meng X, Li N, Sha X, Liu Y, Gao B, Xiao LR, et al. In-situ TEM observations on interaction of basal $\langle a \rangle$ dislocations and β' phases in a Mg–Gd binary alloy. Mater Sci Eng A 2022;841:143017.